Open access • Journal Article • DOI:10.1098/RSTA.1996.0022

# A Laboratory Study of Nonlinear Surface Waves on Water — Source link

Tom E. Baldock, Chris Swan, P. H. Taylor

**Institutions:** Imperial College London, Royal Dutch Shell

**Published on:** 15 Mar 1996 - Philosophical transactions - Royal Society. Mathematical, physical and engineering sciences (The Royal Society)

**Topics:** Wave shoaling, Surface wave, Breaking wave, Wave propagation and Mechanical wave

# A laboratory study of nonlinear surface waves on water

BY T. E. BALDOCK[1], C. SWAN[1] AND P. H. TAYLOR[2].

[1]*Department of Civil Engineering, Imperial College of Science, Technology and Medicine, London SW7 2BU, UK*

[2]*Shell Research BV, Volmerlaan 8, 2288 GD Rijswijk, PO Box 60, The Netherlands*

## Contents



This paper describes an experimental investigation in which a large number of water waves were focused at one point in space and time to produce a large transient wave group. Measurements of the water surface elevation and the underlying kinematics are compared with both a linear wave theory and a second-order solution based on the sum of the wave–wave interactions identified by Longuet–Higgins & Stewart (1960). The data shows that the focusing of wave components produces a highly nonlinear wave group in which the nonlinearity increases with the wave amplitude and reduces with increasing bandwidth. When compared with the first- and second-order solutions, the wave–wave interactions produce a steeper wave envelope in which the central wave crest is higher and narrower, while the adjacent wave troughs are broader and less deep. The water particle kinematics are also strongly nonlinear.

The accumulated experimental data suggest that the formation of a focused wave group involves a significant transfer of energy into both the higher and lower harmonics. This is consistent with an increase in the local energy density, and the development of large velocity gradients near the water surface. Furthermore, the

*Phil. Trans. R. Soc. Lond.* A (1996) **354**, 649–676
*Printed in Great Britain*

nonlinear wave–wave interactions are shown to be fully reversible. However, when compared to a linear solution there is a permanent change in the relative phase of the free waves. This explains the downstream shifting of the focus point (Longuet-Higgins 1974), and appears to be similar to the phase changes which result from the nonlinear interaction of solitons travelling at different velocities (Yuen & Lake 1982).

## 1. Introduction

It is well known that the largest ocean waves do not usually form part of a regular wave train, but represent an individual event within a random sea state. The offshore measurements shown on figure 1 provide a good example of this behaviour. The formation of these very large wave forms is believed to be associated with the focusing of wave components such that the individual wave crests come into phase at one point in space and time. The statistics of extreme waves in a random sea were first investigated by Longuet-Higgins (1952), and the effects of nonlinearity and finite bandwidth further clarified by Longuet-Higgins (1980). More recently, Tromans *et al.* (1991) considered the occurrence of a two-dimensional focused wave group. This solution is based upon the statistical analysis outlined by Slepian (1963) and predicts the most probable extreme wave given the spectral properties of the sea state. Unfortunately, this approach is only valid to a first order of wave steepness and therefore neglects the nonlinear wave–wave interactions. This omission is particularly important in the case of an extreme wave event since (by definition) these waves will be very steep and therefore highly nonlinear.

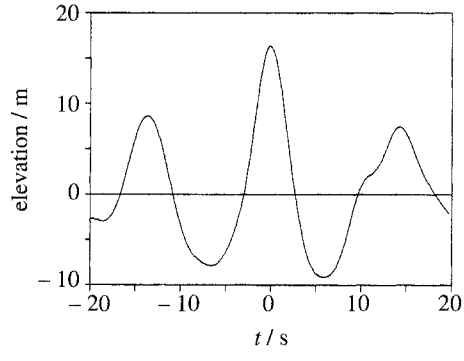


Figure 1. Large ocean wave. (Measurements taken from the Tern Platform located in the northern North Sea. Courtesy of Shell UK Exploration and Production Ltd.).

The importance of the nonlinear interactions was emphasised in an earlier experimental study presented by Rapp & Melville (1990). This considered the breaking criteria associated with a focused wave group, and showed that if $A$ represents the linear sum of the individual wave amplitudes and $k_c$ is the central wave number, wave breaking occurs at much lower values of $Ak_c$ than would otherwise be expected (i.e. $Ak_c \ll 0.4$). This implies that the nonlinear interactions produce a significant increase in both the crest elevation and the underlying kinematics. In general terms, the nonlinear interactions may be subdivided into the high-frequency terms which alter the local characteristics of the wave group (i.e. sharpening of the wave crest and broadening of the wave trough), and the low-frequency terms which correspond

to the global interactions and hence produce the relatively slow changes, such as the perturbation of the mean water level.

The present paper will consider the nonlinear wave–wave interactions, and will present the results of a new experimental study in which the surface elevation, the underlying kinematics and the nonlinearity of the focused wave group were measured within a laboratory wave flume. Section 2 commences with a brief review of the wave–wave interaction theory proposed by Longuet-Higgins & Stewart (1960). These interactions are summed up over a given frequency range to provide a first approximation to the nonlinear interactions occurring within a focused wave group. The experimental apparatus is described in § 3. Section 4 outlines the wave-generation procedure and describes some precautionary observations necessary to ensure the integrity of the resulting data. The experimental observations are discussed in § 5 and comparisons are made with both linear and nonlinear wave theories. Finally, some conclusions are presented in § 6 and the practical implications of the experimental results are briefly outlined.

## 2. Previous work

The first rigorous evaluation of nonlinear wave–wave interactions in water of finite depth was proposed by Longuet-Higgins & Stewart (1960). Using the solution procedure outlined by Stokes (1847), they considered the interaction between two progressive wave trains and produced explicit second-order solutions for both the water surface elevation $\eta$ and the velocity potential $\phi$. If the $x$-axis is measured horizontally in the direction of wave propagation, and the $z$-axis is measured vertically upwards from still water level, the following results apply:

$$\eta = \eta_1 + \eta_2 + \frac{a_1 a_2}{2g}[C\cos(\psi_1 - \psi_2) - D\cos(\psi_1 + \psi_2)], \tag{2.1}$$

$$\phi = \phi_1 + \phi_2 + \frac{E\cosh((k_1 - k_2)(z+h))\sin(\psi_1 - \psi_2)}{g(k_1 - k_2)\sinh((k_1 - k_2)h) - (\sigma_1 - \sigma_2)^2\cosh((k_1 - k_2)h)} - \frac{F\cosh((k_1 + k_2)(z+h))\sin(\psi_1 + \psi_2)}{g(k_1 + k_2)\sinh((k_1 + k_2)h) - (\sigma_1 + \sigma_2)^2\cosh((k_1 + k_2)h)}, \tag{2.2}$$

where the subscripts distinguish between the two wave trains, and $(\eta_1, \eta_2)$ and $(\phi_1, \phi_2)$ are the second-order Stokes solutions expressed in terms of the wave amplitude $a$, the wave number $k$, the wave frequency $\sigma$, the phase angle $\psi$ and the water depth $h$. The constant coefficients ($C$, $D$, $E$ and $F$) are defined by Longuet-Higgins & Stewart (1960) and are reproduced in Appendix A. The $(\psi_1 + \psi_2)$ terms identified in equations (2.1) and (2.2) provide a first approximation to the local nonlinearity discussed earlier, whereas the $(\psi_1 - \psi_2)$ terms correspond to the low-frequency or global interactions.

The solutions proposed by Longuet-Higgins & Stewart (1960) have two important limits. First, if the wave trains are identical ($a_1 = a_2$, $k_1 = k_2$, $\sigma_1 = \sigma_2$ and $\psi_1 = \psi_2$), the resulting wave form will have a first-order surface amplitude of $a = a_1 + a_2$, and the second-order terms must converge to the classical Stokes (1847) solution. Alternatively, if the first wave component is very much shorter than the second ($k_1 \gg k_2$), the classical long-wave–short-wave interaction occurs. In this case, the long wave is unaffected by the short wave, but the short wave is modulated by the

long wave so that it is shorter and higher on the crests of the long wave and longer and lower on the troughs. If $a'$ represents the modulated wave amplitude and $k'$ the modulated wave number, Longuet-Higgins & Stewart (1960) give the limiting results as

$$a' = a_1 + a_1 a_2 k_2 (\tfrac{1}{4} \tanh(k_2 h) + \tfrac{3}{4} \coth(k_s h)) \cos(\psi_2), \tag{2.3}$$

$$k' = k_1 + a_2 k_1 k_2 \coth(k_2 h) \cos(\psi_2). \tag{2.4}$$

Numerical calculations conducted by Longuet-Higgins (1987) show good agreement with equations (2.3) and (2.4) provided neither of the wave trains are too steep. However, as the wave steepness increases the numerical results diverge from the second-order solution. This indicates the increasing importance of the higher order terms. A similar pattern has been observed in laboratory measurements presented by Miller *et al.* (1991).

If equations (2.1) and (2.2) are applied to a focused wave group, the total second-order solution is given by the sum of the interactions resulting from each pair of wave components. If a wave group consists of $N$ free waves, the second-order description of the surface elevation and the velocity potential are, respectively,

$$\eta = \sum_{n=1}^{N} \eta_{(n)} + \sum_{n=1}^{N} \sum_{m=n+1}^{N} \eta_{(n,m)}, \tag{2.5}$$

$$\phi = \sum_{n=1}^{N} \phi_{(n)} + \sum_{n=1}^{N} \sum_{m=n+1}^{N} \phi_{(n,m)}, \tag{2.6}$$

where $\eta_{(n)}$ and $\phi_{(n)}$ are the second-order Stokes solutions for the $n$th wave component, and $\eta_{(n,m)}$ and $\phi_{(n,m)}$ are the second-order interactions between the $n$th and $m$th components of the wave group. These latter terms are calculated using equations (2.1) and (2.2). Equations (2.5) and (2.6) provide a first approximation to the nonlinear interactions occurring within a focused wave group. It is these solutions which will be compared to the experimental data.

## 3. Experimental apparatus

### (*a*) *Laboratory flume*

The experiments were conducted in a new wave flume which has been constructed in the Civil Engineering Hydraulics laboratory at Imperial College. This facility is 20 m long, 0.3 m wide and has a maximum working depth of 0.7 m. The side walls, and the central portion of the bed, are constructed from glass for maximum optical access. The waves are generated by a flat bottom-hinged paddle located at one end of the wave flume. The hydrostatic loads acting on the paddle are supported mechanically (via a system of springs and pulleys), and the drive motor is controlled numerically. This arrangement allows the successful generation of waves with a period range from 0.4 to 2.0 s.

Although the paddle mechanism has an 'active feedback response', whereby a reflected wave component is detected by a force transducer and absorbed during the generation process, the success of the present study was dependent upon the effective absorption of the wave energy at the downstream end of the wave flume. No reflected wave components could be tolerated within the working section of the wave flume. To achieve this a large block of poly-ether foam (hole gauge 2 mm) was installed to

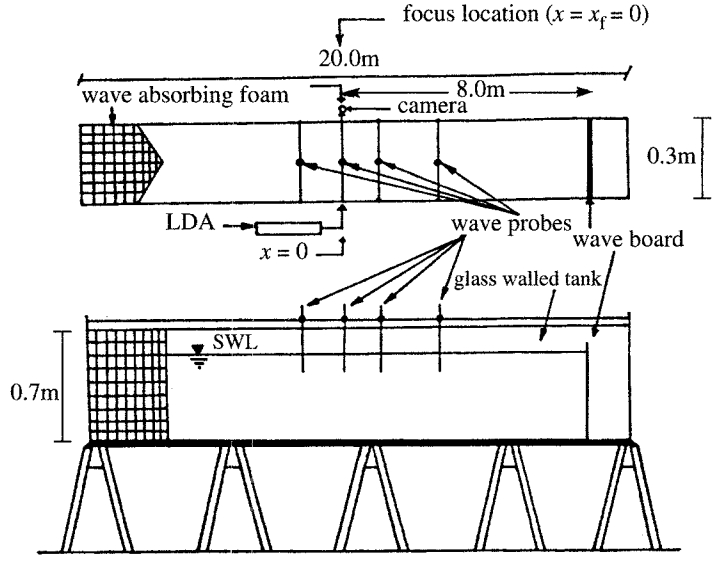


Figure 2. Experimental apparatus.

provide passive absorption. The foam was 2 m in length and the leading edge was cut to form a vertical wedge with an included angle of approximately 30°. A sketch showing the layout of the experimental flume is given in figure 2.

### (*b*) *Measuring techniques*

A total of six surface-piercing wave gauges were used to measure the time history of the water surface elevation at fixed spatial locations. These gauges consist of two vertical wires 0.8 mm in diameter and located 10 mm apart. Each gauge was mounted on a vertical traverse attached to a movable carriage located on rails at the top of the wave flume. The output from these gauges is directly proportional to their depth of immersion. This allows the water surface elevation to be determined to within ±1 mm with minimal disturbance of the flow field.

The wave kinematics were measured using laser Doppler anemometry. A 35 mW helium-neon laser was used to create a two-beam arrangement from which the horizontal component of the wave-induced velocity was determined. The laser beams were initially projected in a horizontal direction and existed in a vertical plane parallel to the centre line of the wave flume. After reflection in an optically flat mirror, orientated at 45° to the horizontal, the beams were directed vertically upwards. A second mirror was used to create a 90° reflection and rotation, so the beams were perpendicular to the direction of wave motion and orientated in a horizontal plane. Finally, a 500 mm focal length converging lens was used to create a measuring volume which was located midway across the width of the tank, and estimated to be approximately 0.5 $mm^3$. The receiving camera and the associated photomultipliers were located on the opposite side of the wave tank so that the intersection of the two beams could be observed in 'forward scatter' mode. This arrangement provides the optimal signal-to-noise ratio with no disturbance of the flow field.

To position the measuring volume at any depth within the flow field, the second deflecting mirror, the converging lens and the receiving camera were supported within a traverse mechanism. The positional accuracy of this arrangement was estimated

to be ±1 mm in the vertical direction and ±2 mm in the horizontal direction. To improve the output signal from the laser Doppler anemometer, the flow was seeded with milk added in the ratio of approximately 100 ppm. After filtering to remove some high-frequency contamination (> 60 Hz), it was estimated that the horizontal velocity could be determined to ±2% with the accuracy largely being dependent upon the calibration of the frequency tracker, and the measurement of the beam separation.

The calibration of the laser Doppler anemometer was further checked by measuring the horizontal velocities beneath a series of regular waves. To eliminate the unknown return flow (Swan 1990), the velocity amplitude was calculated at a large number of elevations beneath the level of the wave trough. These results were compared with a fifth-order Stokes solution based upon the formulation proposed by Fenton (1985). The agreement was near perfect, with maximum errors close to the accuracy noted above (±2%).

## 4. Experimental method

### (a) *Wave generation*

To create a desired wave group within the laboratory flume, a specified range of wave components were generated and their relative phases adjusted so that, at some instant in time, the individual wave components were brought into focus at one spatial location. Constructive interference occurs and a large wave crest results. This approach is similar to that adopted by Rapp & Melville (1990) in that a linear wave solution is used to determine the appropriate phasing of the various wave components. If the $n$th wave component has a wave number $k_n$ $(2\pi/L_n)$ and a wave frequency $\sigma_n$ $(2\pi/T_n)$, where $L_n$ and $T_n$ are, respectively, the wave length and the wave period, the surface elevation $\eta$ at the focal point $(x = x_f)$is given by

$$\eta(x_f, t_f) = \sum_{n=1}^{N} a_n \cos(k_n x_f - \sigma_n t_f), \tag{4.1}$$

where $N$ is the total number of wave components, $a_n$ is the amplitude of the $n$th wave and $t_f$ is the time at which the wave focusing occurs. If the Cartesian coordinates shown in figure 2 have their origin at the focus position $(x_f = 0)$ then the individual wave components are focused at $t_f = 0$, and a linear wave solution gives the required surface elevation generated at the wave paddle $(x = x_p)$ as

$$\eta(x_p, t) = \sum_{n=1}^{N} a_n \cos(k_n x_p - \sigma_n t), \tag{4.2}$$

where $x_p$ is the linear predicted distance from the focal point to the wave paddle.

Since this approach is based upon the linear sum of the individual wave components, it neglects the nonlinear wave–wave interactions. As a result, both the focal point and the focus time are unknown. To simplify the experimental procedure, the focus point $(x = x_f)$ was predetermined so that the focused wave occurred 8 m downstream of the paddle (figure 2). This enabled both the velocity data and the transfer function (see below) to be measured at the same cross section. To achieve this, the input value of $x_p$ was determined experimentally for each wave group. Using this approach, the focusing time $t_f$ could be set to zero and a direct comparison made with the solutions given in equations (2.5) and (2.6).

The generation of a desired wave group (with a given spectral content) is dependent upon the accuracy of the transfer function. This describes the relationship between the numerically generated input signal and the resulting surface elevation. If $I(\sigma)$ represents the amplitude of a sinusoidal input signal with a wave frequency $\sigma$, and $a(\sigma)$ is the amplitude of the surface profile measured at the focus position, then a first-order transfer function $T(a, \sigma)$ is defined by

$$a(\sigma) = T(a, \sigma)I(\sigma). \tag{4.3}$$

To avoid the uncertainty associated with a theoretically predicted transfer function based upon the response of the paddle control, $T(a, \sigma)$ was determined experimentally using an appropriate range ($0.4\,\mathrm{s} < T < 2.0\,\mathrm{s}$) of regular wave trains. This calibration was repeated at regular intervals throughout the experimental study and the transfer function found to be extremely stable. The maximum RMS error in the predicted water surface elevation for any one wave component was never greater than 2%. This is consistent with the measuring error associated with the surface piercing wave gauges ($\pm 1$ mm). It should be noted that no attempt was made in the present study to investigate the higher order characteristics of the transfer function (Schaffer 1993). This is consistent with the widely held belief that a bottom hinged paddle operating in deep water produces no significant unwanted higher order harmonics. Indeed, if this were not the case, the water surface elevation and the velocity measurements beneath a regular wave train would have shown considerable departures from the classical Stokes solution. No such discrepancies were observed.

### (*b*) *Preliminary observations*

If the simultaneous generation of a large number of individual wave components is to be successfully completed within a laboratory wave flume, precautions must be taken to limit the following difficulties:

(1) the reflection of the long wave components at the downstream end of the wave flume;

(2) The modulation of the short wave components and the formation of cross tank resonance;

(3) The development of longitudinal seiching due to the start-up characteristics of the wave paddle.

A series of preliminary observations were conducted to investigate these effects. First, the spatial uniformity of an appropriate range of regular wave trains was measured over the central portion of the wave flume, and the reflection coefficient determined from the variation in wave height. The passive absorber shown in figure 2 was found to work remarkably well. In the present study, the longest wave component included in any wave group had a period of $T = 1.6$ s. At this, and all other wave periods, the reflection coefficient was less than 2%. At the other end of the wave spectrum, the generation of high-frequency wave components may induce a transverse oscillation across the width of the wave flume. This is often coupled with a downstream modulation of the surface profile. Although these effects were reduced by the width of the experimental facility (0.3 m), some difficulties were observed for wave periods less than 0.5 s. To eliminate this effect, the shortest wave components were restricted to $T \geqslant 0.5$ s. In this case, the surface elevation corresponding to a regular wave train ($T = 0.5$ s) measured at $x = x_f$ showed no evidence of either wave modulation or cross-tank resonance. Indeed, at this, and all other wave periods, the variation in the wave height was less than 1%.

Finally, to limit the disturbance created by the start-up of the wave paddle, the amplitude of the input signal was linearly increased from zero over the first 4 s of the generation process. To assess the effectiveness of this approach, the water surface elevation was measured at the downstream end of the wave flume during the initial generation of a large regular wave train. Several wave periods were investigated ($0.5\,\mathrm{s} < T < 1.5\,\mathrm{s}$), and in no case was there any significant evidence of longitudinal seiching (i.e. the amplitude of any long-wave components was always less than the measuring accuracy of the wave gauges, $\pm 1$ mm). However, in each case, the envelope of the advancing wave front was similar to the Fresnel envelope first investigated by Longuet-Higgins (1974). In the present investigation, this initial amplitude variation has no effect upon the nature of the focused wave group since the individual wave components were simultaneously generated (see later) for a period of 30 s prior to the formation of the focused event.

In conducting these preliminary tests, two further difficulties arose. First, the high-frequency wave components decayed significantly along the length of the wave flume. Although the transfer function was calibrated for wave heights measured at the focus position, this decay represents an additional spatial dependence which was undesirable within the present investigation. The addition of a photographic wetting agent, (Teepol, in approximately 1 ppm) produced a reduction in the surface tension and helped to limit the effects of the side walls. After the inclusion of this additive, the decay of the shortest wave components ($T = 0.5$ s) within the envelope of the focused wave group (say 5–6 m) was found to be less than 2% of the generated wave height. This approach also eliminated any small disturbances on the water surface.

The second problem was again associated with the effects of wall friction. During the propagation of a focused wave group, the maximum water surface elevation corresponds to an individual event within the wave flume. The largest wave crest therefore propagates along previously dry side walls. This enhances the frictional effect and produces a slight three dimensionality of the surface profile. To minimize this, the side walls were sprayed with a water–Teepol mixture before the generation of each wave group. Subsequent measurements showed that the variation in the surface elevation across the width of the wave flume was always less than 2%.

## 5. Experimental results

The experimental investigation considered the four period ranges or frequency bands indicated on table 1. Each wave group consisted of 29 individual wave components, which were simultaneously generated by the wave paddle. In each case, the wave components were of equal amplitude, and equally spaced within the appropriate period range. This does not, however, correspond to a uniform spacing within the frequency domain, and, consequently, the amplitude spectrum, $a(\sigma)$, derived from a fast Fourier transform of the input signal decays according to $\sigma^{-2}$. This is in marked contrast to the 'top hat' spectrum used by Rapp & Melville (1990) in their study of wave breaking.

To complete the test conditions, a range of input amplitudes were considered. This allowed each frequency band to be investigated up to the limiting condition where wave breaking occurs. As a result, a total of some 45 individual wave groups were investigated within the present study.

Table 1. *Input characteristics*

| case | period range (s) | frequency band (Hz) |
|---|---|---|
| A | $0.5 \leqslant T \leqslant 1.5$ | $0.66 \leqslant f \leqslant 2.0$ |
| B | $0.6 \leqslant T \leqslant 1.4$ | $0.71 \leqslant f \leqslant 1.66$ |
| C | $0.7 \leqslant T \leqslant 1.3$ | $0.77 \leqslant f \leqslant 1.42$ |
| D | $0.8 \leqslant T \leqslant 1.2$ | $0.83 \leqslant f \leqslant 1.25$ |

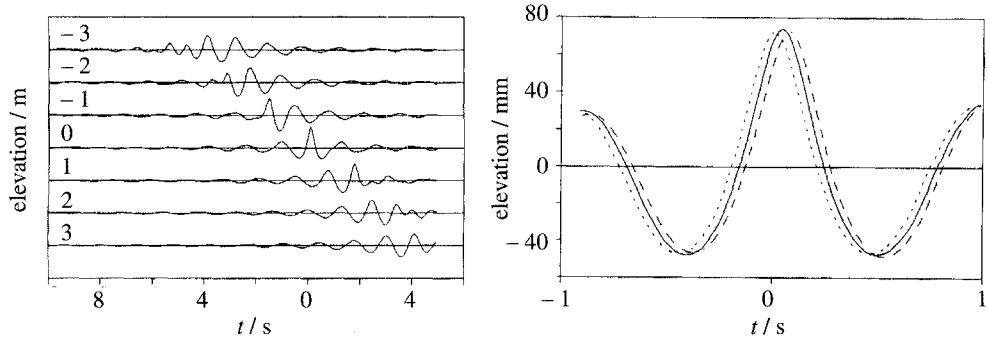


Figure 3. (*a*) The formation of a focused wave group. The number indicated on the left-hand side corresponds to the position along the length of the wave flume, $x(m)$. (*b*) Wave focusing close to the focal point: - - - -, $x = -10$ mm; ——, $x = 0$ mm; – – –, $x = +10$ mm.

### (*a*) *Evolution of a focused wave group*

The evolution of a focused wave group is considered in figure 3*a*. These measurements correspond to case B in table 1 and show the time history of the surface elevation at seven spatial locations. If the origin of the coordinate axes is established at the focus position ($x_f = 0$), the measuring locations are $x = -3$ m, $-2$ m, $-1$ m, 0 m, 1 m, 2 m and 3 m where $x$ is measured in the direction of wave propagation. Figure 3*a* shows the convergence of wave energy at the focal location and the rapid development of the maximum crest elevation.

Figure 3*b* considers the development of the wave group close to the focal location. The measurements correspond to case D and show surface elevations recorded at $x = -10$ mm, 0 and $+10$ mm. The maximum crest elevation clearly arises at the focal location ($x = 0$), and the water surface elevation $h(t)$ is symmetrical about the focusing event. At the adjacent locations ($x = -10$ mm and $+10$ mm), the crest elevation is reduced, and the surface profile is asymmetrical. Measurements of this type were used to determine the location of the focus position for each of the wave groups investigated in the present study.

The reversibility of the water surface elevation is considered in figures 4*a–c*. In each figure, the time history of the water surface elevation at equal distances upstream ($-x$) and downstream ($+x$) of the empirically determined focus position are presented. However, at the downstream location ($x > 0$), the time history has been reversed (i.e. $\eta(-t)$), so that in each case ($x = \pm 1$ m, $\pm 2$ m and $\pm 4$ m) two comparable plots are presented. Although this data specifically corresponds to the narrow-banded spectrum (case D) with an input amplitude of $A = 55$ mm, these results are representative of all the wave groups generated in the present study. It

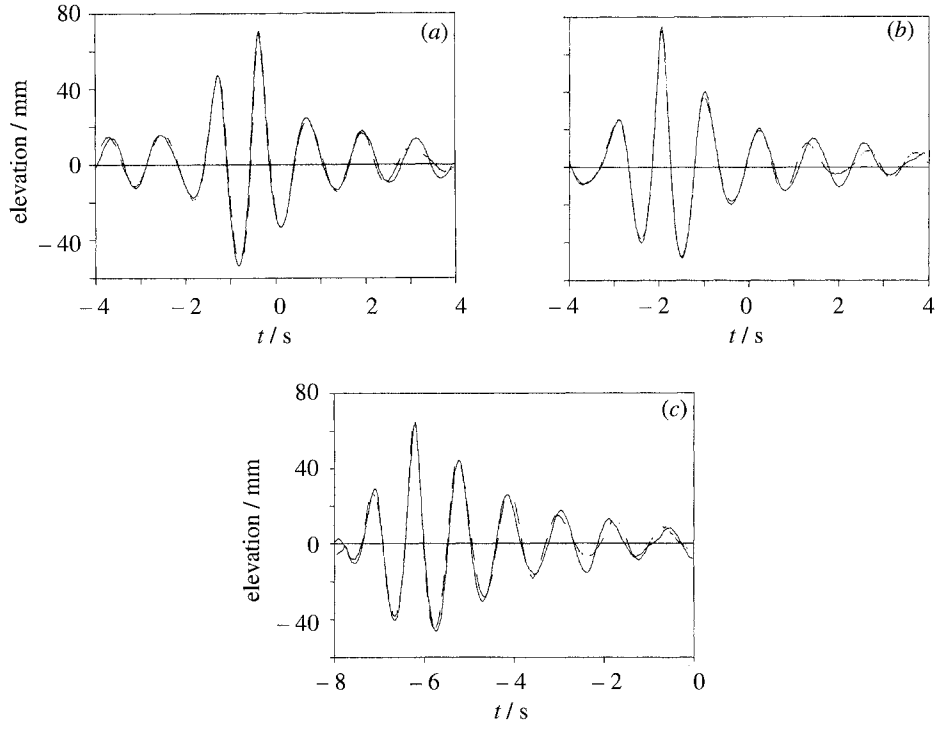


Figure 4. Reversibility of the water surface elevation either side of the focus point ((*a*) $x = \pm 1$ m; (*b*) $\pm 2$ m; (*c*) $\pm 4$ m): ——, $\eta(t)$ at $x < 0$; — - —, $\eta(-t)$ at $x > 0$.

is clear from this data that the water surface elevation either side of the focus point is virtually identical, and thus the wave group is symmetric in both space and time. This implies that the nonlinear wave–wave interactions are fully reversible, provided viscous effects are neglected and wave breaking does not occur.

### (*b*) *Surface elevation at the focal location*

Figures 5 and 6 concern the surface elevations resulting from the broad-banded spectrum (case B) and the narrow-banded spectrum (case D). Three input wave amplitudes are considered ($A = 22$ mm, 38 mm and 55 mm), where $A$ represents the linear sum of the component wave amplitudes ($A = 29a_n$). In each figure, the surface elevation measured at the focus point is compared with the first-order solution derived from the linear sum of the individual wave components. With the smallest input amplitude (figures 5*a* and 6*a*), there is good agreement between the experimental data and the linear solution. In both cases the amplitude of the individual wave components is less than 1 mm (i.e. $a_n = 22/29$ mm) and, consequently, the nonlinear wave–wave interactions are almost non-existent. Figures 5*b*, 6*b* and 5*c*, 6*c* concern the larger input amplitudes ($A = 38$ mm and 55 mm). In these figures the increased wave amplitude produces a rapid divergence from the linear solution. The wave crest at the focus position becomes higher and narrower, while the adjacent wave troughs become wider and less deep. The nonlinearity therefore creates a steeper wave envelope. This is consistent with a local increase in the energy density due to a transfer of energy into the higher harmonics.

The effect of the nonlinear interactions is largest in the narrow-banded spectrum

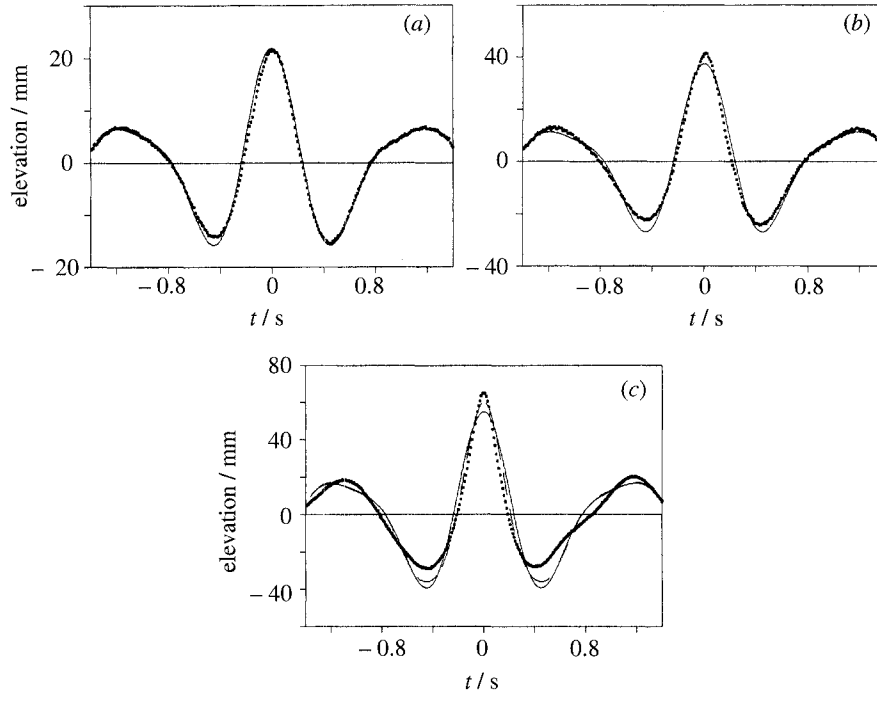


Figure 5. Surface profile at the focal point (case B, (*a*)$A = 22$ mm; (*b*) $A = 38$ mm; (*c*) $A = 55$ mm): •, measured data; ——, linear solution; — —, second-order solution.

(case D). With an input amplitude of $A = 55$ mm (figure 6*c*), the crest elevation measured relative to still water level is 30% larger than the linear solution and 20% larger than the second-order solution. These results are in marked contrast to the equivalent values for a regular wave, where, even at the limiting condition (i.e. $ak \approx 0.4$), the maximum crest elevation is only some 5% larger than the second-order Stokes solution. The importance of the higher order interactions is consistent with the numerical calculations presented by Longuet-Higgins (1987). After reconsidering the long-wave–short-wave interaction, he showed that the second-order solution will underestimate the nonlinearity as the wave steepness increases. The present observations appear to confirm this trend, and suggest that, in the case of a focused wave group, the higher order interactions develop rapidly and therefore occur at a relatively low wave steepness.

The maximum crest elevation is considered in figure 7. The vertical axis defines the crest elevation measured at the focus position, and the horizontal axis describes the linear solution based upon the input signal sent to the wave paddle. The experimental data corresponds to the four frequency bands given in table 1 and shows that the nonlinear wave–wave interactions increase with the input amplitude, and reduce with increasing bandwidth. The relationship between the bandwidth and the maximum crest elevation is further considered in figure 8. The four frequency ranges described in table 1 are again considered and the crest elevations resulting from three input amplitudes ($A = 20$ mm, 40 mm and 55 mm) are compared with the second-order solution given in equation (2.5). It is interesting to note that over this (admittedly) limited range of frequency bands, the predicted second-order crest elevations are independent of the bandwidth. In contrast, the experimental data are

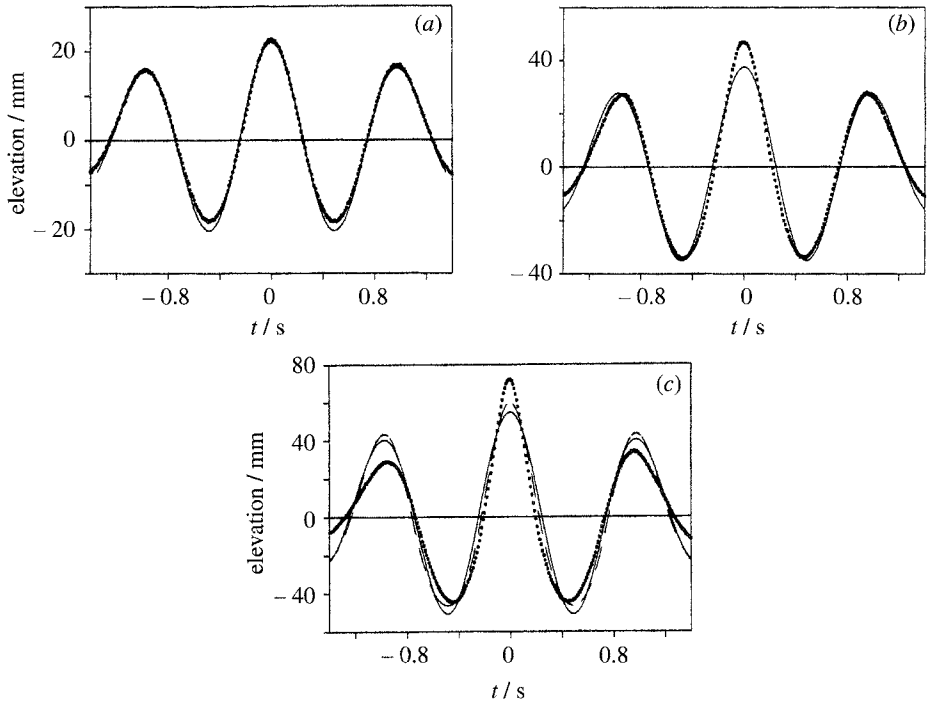


Figure 6. Surface profile at the focal point (case D, (*a*) $A = 22$ mm; (*b*) $A = 38$ mm; (*c*) $A = 55$ mm): •, measured data; ——, linear solution; — —, second-order solution.

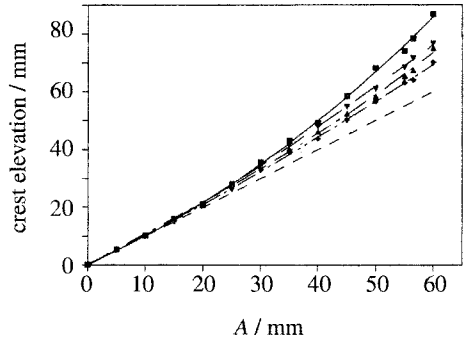


Figure 7. Measured crest elevations: – – –, linear solution; — - - —, case A; — - —, case B; — —, case C; ——, case D.

strongly bandwidth dependent, and show that the largest nonlinear wave–wave interactions occur in the narrow-banded spectrum (case D). This comparison highlights the importance of the higher order wave–wave interactions, and implies that the bandwidth dependence arises at order $a_n^3 k_n^3$ and above.

### (*c*) *Nonlinearity and focus location*

The large increase in the crest elevation of the narrow-banded spectrum (case D) prompted a further investigation into the nonlinearity of a focused wave group. By inverting the input signal $I(t)$ sent to the paddle (i.e. $-I(t)$), the surface elevation generated at the focus position will correspond to the summation of $N$ wave troughs

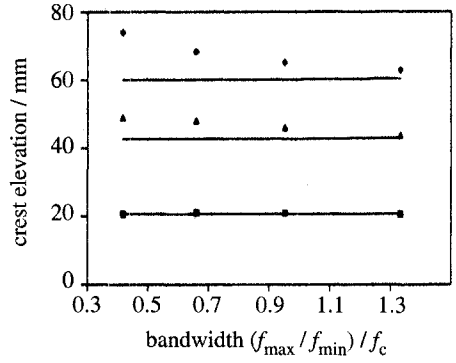


Figure 8. Crest elevation and bandwidth dependence: ——, second-order solution; ■, $A = 20$ mm; ▲, $A = 40$ mm; ♦, $A = 55$ mm.

rather than $N$ wave crests. If the development of a focused wave group is essentially a linear process, the surface elevation, $\eta^*(t)$, resulting from the negative input signal will represent the inverse of the original surface profile (i.e. $-\eta^*(t) = h(t)$). However, if the focusing process is nonlinear, neither the local nor the global second-order interactions ($\propto (ak)^2$) identified in equation (2.1) will change sign when the wave group is inverted. In consequence, if the water surface profile corresponding to the sum of $N$ wave troughs is itself inverted (i.e. $-\eta^*(t)$), it will differ from the profile arising due to the summation of $N$ wave crests ($\eta(t)$). This effect, and, in particular, the local nonlinearity resulting from the high-frequency interactions, may be expected to increase the amplitude of the wave group.

The present results, corresponding to the narrow-banded spectrum (case D), are given in figures 9*a–d*. For each input amplitude, the focus position for the positive and negative input signals were identical, and the difference between the recorded water surface elevations ($\eta(t)$ and $-\eta^*(t)$) provides a measure of the nonlinearity of the wave group. In figure 9*a*, ($A = 12.5$ mm) the surface profiles are almost identical. This corresponds to the case where the individual wave components are very small ($a_n <$ 0.5 mm) and, consequently, the wave–wave interactions are negligible. However, an increase in the input amplitude (i.e. $A = 25$ mm, 38 mm and 50 mm) highlights the nonlinear behaviour of the wave group. The increasing difference between the measured surface profiles would appear to substantiate the nonlinearity observed in figures 5–7.

The position and time of the focusing event were also found to be dependent upon the nonlinearity of the wave group. In a further series of tests the linear solution ($x_p = 8$ m) was adopted and the exact position of the focus point determined experimentally (i.e. $x_f \neq 0$, $t_f \neq 0$). The four frequency bands described in table 1 were considered, and in each case it was found that an increase in the wave amplitude produced a downstream shift of the focus point. This effect was first noted by Longuet-Higgins (1974), and further reported (without rigorous investigation) by Kim *et al.* (1992). The present results describing the downstream shifting of the focus point are given in figure 10*a*, while the corresponding data describing the focus time are given on figure 10*b*. In this latter case there appears to be considerable scatter in the experimental data. This is undoubtedly due to the accuracy (±0.05 s) of the internal (PC) clock used for the numerical control of the wave paddle. Although the drive signals were highly repeatable, the accuracy of the clock produced small variations in the start-up time of the wave paddle. This variability has no bearing on

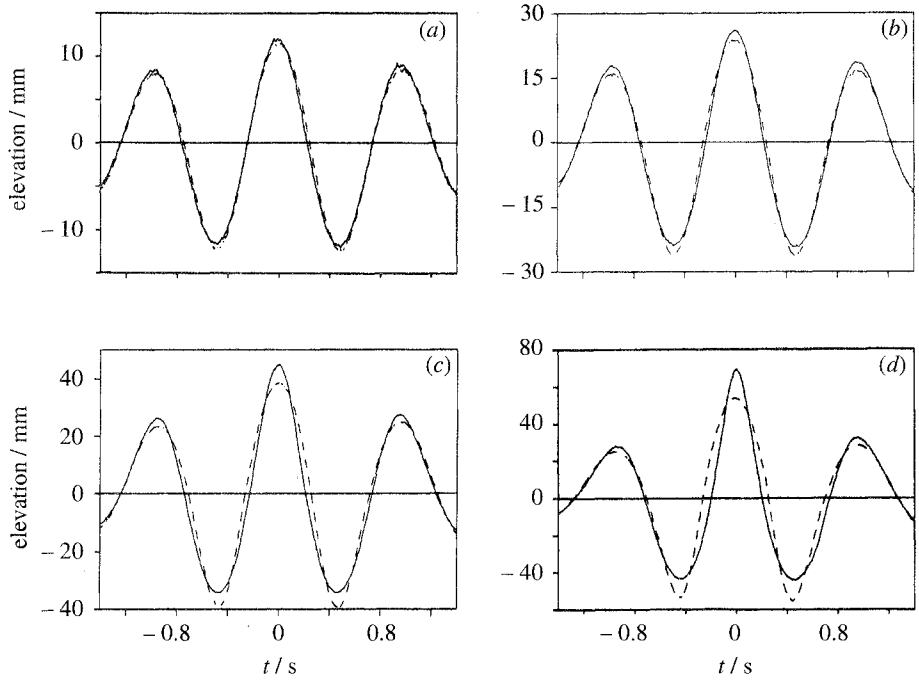


Figure 9. Measured surface profiles (case D, (*a*) $A = 12.5$ mm; (*b*) $A = 25$ mm; (*c*) $A = 38$ mm; (*d*) $A = 50$ mm): ——, $\eta(I[t])$; – – –, $-\eta^*(-I[t])$.

the spatial location of the focused wave group. The data presented in figures 10*a*, *b* suggest that both the location and time of the focused event are dependent upon the nonlinearity of the wave group. In each case, $x$ and $t$ increases with the input amplitude, but reduces with increasing bandwidth. This is consistent with the observations of the maximum crest elevation shown in figures 7 and 8. The experimental data shown in figures 9*a*–*d* indicate that the summation of $N$ wave troughs are focused at exactly the same location as $N$ wave crests. This result indicates that the change in the position of the focus point is not dependent upon the local nonlinearity, but is dependent upon the global interactions and the overall nonlinearity of the wave group.

### (*d*) *Wave kinematics*

The horizontal component of the wave-induced water-particle velocity was measured at the focus location using the laser Doppler anemometer described previously. This method provides velocity data at a single point, and, consequently, a large number of repeated generations of the same wave group were necessary to achieve a description of the entire flow field. For this approach to be satisfactory, the paddle mechanism must be capable of repeatedly generating an identical wave group at the same location within the wave flume. Tests conducted over a long time period for a wide range of frequency bands showed that a particular surface profile could be consistently repeated. To complete the kinematic measurements, wave groups B and D were generated approximately 400 times. The standard deviation of the measured crest elevations was 2.1%. This is consistent with the measuring errors associated with the wave gauges.

A typical sequence of velocity traces and surface profiles are shown in figures 11*a*, *b*.

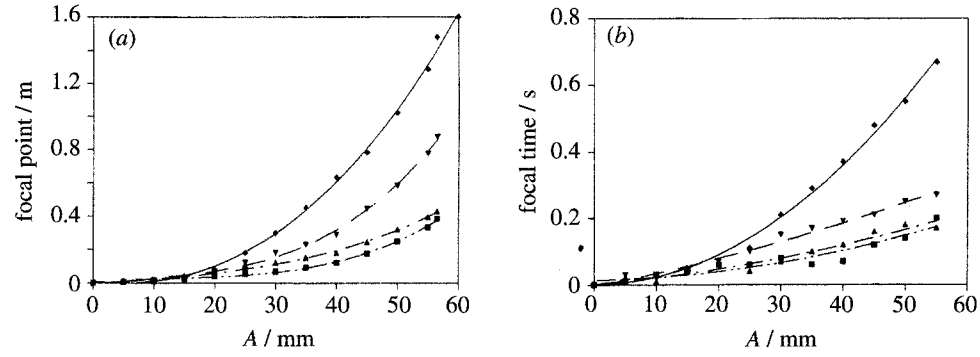


Figure 10. (*a*) Position of the focal point: — - - —, case A; — - —, case B; — —, case C; ——, case D. (*b*) Time of focusing (at $x = x_f$): — - - —, case A; — - —, case B; — —, case C; ——, case D.

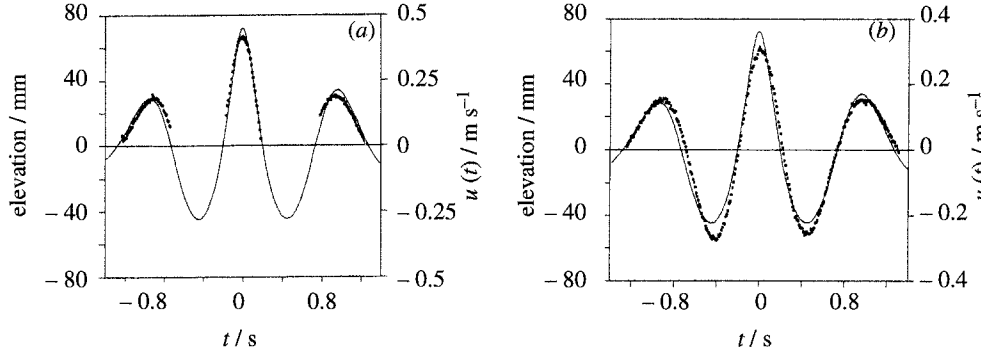


Figure 11. Horizontal velocity (case D, $A = 55$ mm; (*a*) $z = 0$ mm; (*b*) $z = -60$ mm): ——, surface elevation $\eta(t)$; •, horizontal velocity $u(t)$.

These measurements correspond to the narrow-banded spectrum (case D) and show the time history of the horizontal velocity at two elevations ($z = 0$ mm and $z = -60$ mm) directly beneath the focus location. Figure 11*a* provides measurements taken above trough level and, consequently, the velocity trace is intermittent. Using the measuring system discussed previously, the velocity field could be determined to within 8 mm of the water surface. Above this level the velocity trace was of insufficient duration to be reliably tracked by the laser Doppler signal processor.

The horizontal velocity measured beneath the broad-banded spectrum (case B) and the narrow-banded spectrum (case D) are shown in figures 12 and 13, respectively. In each case, three input amplitudes are considered ($A = 22$ mm, 38 mm and 55 mm) and the measurements compared with both the linear and the second-order solutions. At the lowest value of the wave steepness ($Ak_c \approx 0.1$), there is good agreement between the observed and predicted kinematics (figures 12*a* and 13*a*). However, at $Ak_c \approx 0.15$ (figures 12*b* and 13*b*), the nonlinear effects are significant. In the broad-banded spectrum (case B), the maximum horizontal velocity occurring at the focus location ($x = 0$, $t = 0$) is reduced due to the set-down under the wave group. This effect is caused by a long bound wave associated with the $(\psi_1 - \psi_2)$ terms discussed earlier. The resulting motion, which first arises at a second order of wave steepness (Longuet-Higgins & Stewart 1960, 1964), takes the form of a backwards (or negative) flow on the scale of the wave group. Indeed, it may be interpreted as a dynamic response to the positive mass transport occurring within the wave group. However,

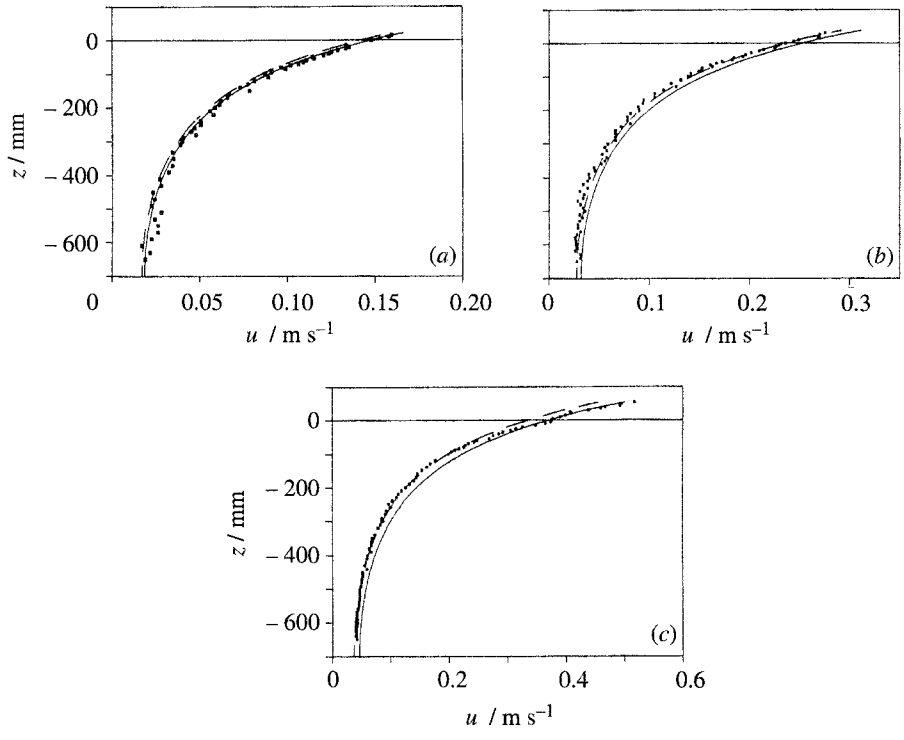


Figure 12. Horizontal velocity beneath the focal point (case B, (*a*) $A = 22$ mm; (*v*) $A = 38$ mm; (*c*) $A = 55$ mm): •, measured data; ——, linear solution; — —, second-order solution.

since a focused wave group represents a transient event, the backwards flow is time-dependent (i.e. a bound long wave) and should not therefore be misinterpreted as the time-independent second-order Stokes drift (or the resulting Eulerian backflow) which arises beneath a regular wave train.

Figure 12*b* shows good agreement between the second-order solution and the velocity profile measured beneath the broad-banded spectrum. In the narrow-banded spectrum (figure 13*b*), the velocity reduction is smaller and can only be identified in the lower layers of the flow field (i.e. $z \leqslant -200$ mm). Close to the water surface ($z \geqslant -100$ mm) the measured velocity is either larger than or equal to the linear solution. These observations suggest that the nonlinear interactions occurring at order $a_n^3 k_n^3$ and above are already becoming significant in the narrow-banded spectrum.

A further increase in the wave steepness ($Ak_c \approx 0.22$) produces a highly nonlinear flow field. In the broad-banded spectrum (figure 12*c*), the second-order velocity reduction is clearly present in the lower layers of the flow field ($z \leqslant -100$ mm). However, above this level the velocity increases so that the values recorded near the water surface are larger than the predicted second-order motion (equation (2.6)). In the narrow-banded spectrum (figure 13*c*), the higher order interactions are very significant. The second-order velocity reduction may be present in the lower layers of the flow field, but the velocity increases very rapidly towards the water surface. Indeed, the velocities recorded within the crest of the focused wave group are 30% larger than either the second-order solution or the extrapolated linear solution. The gradient of the horizontal velocity within this region (i.e. $\partial u/\partial z$ as $z \rightarrow \eta$) is also

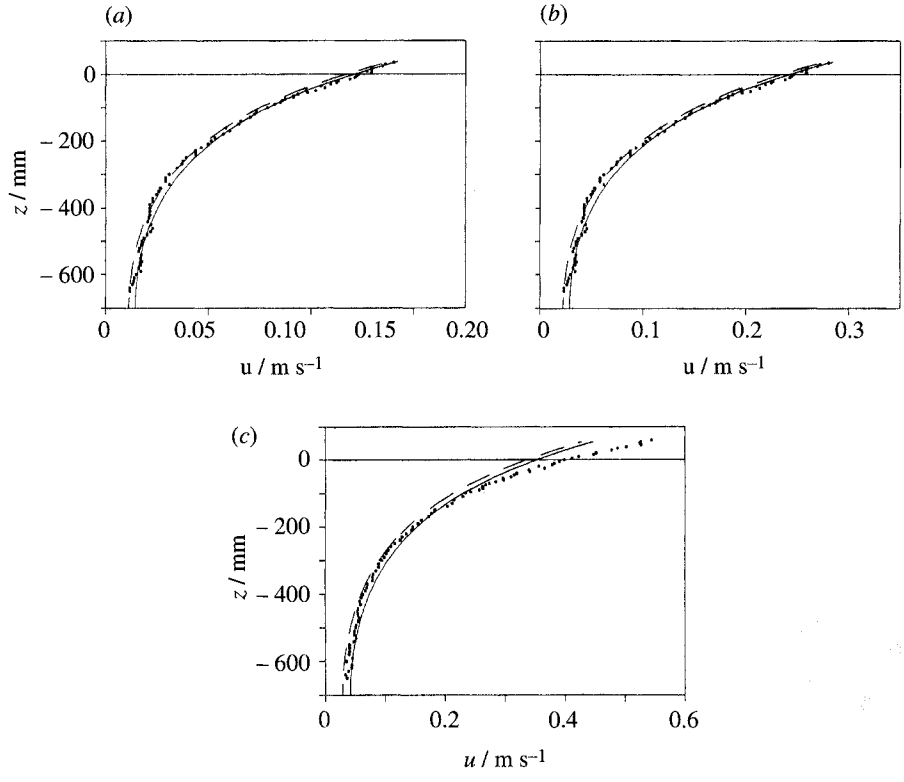


Figure 13. Horizontal velocity beneath the focal point (case D, (*a*) $A = 22$ mm; (*b*) $A = 38$ mm; (*c*) $A = 55$ mm): •, measured data; ——, linear solution; — —, second-order solution.

considerable larger than that predicted by a linear solution. This suggests a transfer of energy to wave components of greater frequency and shorter wavelength.

It is important to note that, in the case of large amplitude waves, the application of a linear solution above still water level ($z = 0$) is known to produce significant errors. This is because, in a linear solution, the velocity due to the short-wave components will be extrapolated to the crest of the longer waves. In essence, these difficulties arise because the extrapolation process does not allow the individual wave components to ride over one another. The resulting errors are often referred to as 'high-frequency contamination' (Sobey 1990) and have been discussed by a number of authors including Forristall (1986), Gudmestad (1990) and Taylor (1992). It is widely believed that the use of an extrapolated linear solution in a random sea state will overestimate the magnitude of the crest kinematics (Skjelbreia *et al.* 1991). Indeed, a number of empirically modified wave theories have been proposed to overcome exactly this difficulty (Wheeler 1970; Rodenbusch & Forristall 1986; Gudmestad & Connor 1986). However, the present measurements indicate that this overestimation does not necessarily arise when the solution is based on the correct linear wave amplitudes. Indeed, in the case of a focused wave group, the present measurements suggest that the non-

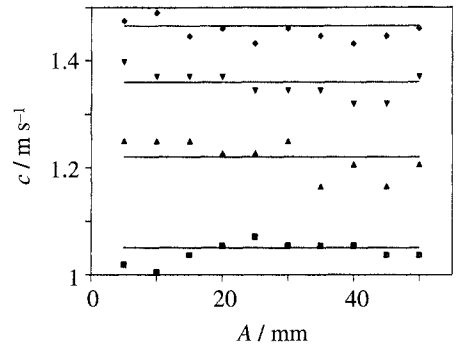


Figure 14. Velocity of the focused wave crest ($V_{cf}$): ■, case A; ▲, case B; ▼, case C; ♦, case D; ——, linear solution.

linear interactions can produce near-surface velocities which are significantly larger than an extrapolated linear solution.

### (e) *Crest velocity and onset of wave breaking*

If the position of an individual wave crest is given by $\partial\eta/\partial x = 0$ and occurs at $x = x_c$, the phase velocity of the focused wave crest ($V_{fc}$) is defined by

$$V_{fc} = \mathrm{d}x_c/\mathrm{d}t \quad \text{at } x_c = 0, \quad t = 0. \tag{5.1}$$

At a first order of wave steepness, equation (5.1) yields a solution of the form

$$(V_{fc})_{linear} = \sum_{n=1}^{N} a_n \sigma_n k_n \Big/ \sum_{n=1}^{N} a_n k_n^2. \tag{5.2}$$

Figure 14 compares this solution with the experimental data gathered from two wave gauges located either side of the focus position. If $\Delta x$ is the separation of the probes (in this case 300 mm) and $\Delta t$ is the time taken for the largest wave crest to pass between the probes, the experimental data shown on figure 14 simply corresponds to $\Delta x/\Delta t$. Using this approach, it was estimated that the phase velocity of the focused wave crest could be determined to ±3%.

For each frequency range (cases A–D), the measured data is shown to be in good agreement with the linear solution given in equation (5.2). In particular, the phase velocity of the focused wave crest appears to be independent of the wave amplitude and does not display the nonlinearity observed in either the water surface elevation or the underlying kinematics. This may, in part, reflect the fact that the increase in the phase velocity due to the nonlinearity of the wave form is generally small. For example, in the case of a regular wave train with a steepness of $ak = 0.25$, the nonlinear increase in the phase velocity is only of the order of 3%. However, in the present case, each frequency band has been investigated up to the point of wave breaking, and one might therefore expect the local nonlinearities to increase the focused phase velocity by a significant factor. Indeed, Kinsman (1984) has shown that the limiting crest velocity in a regular wave train is approximately 10% larger

than the first-order solution. If $a_f$, $k_f$ and $c_{f1}$ are the local wave amplitude (or half the instantaneous wave height), the local wave number, and the linear phase velocity at the focus point, then (to a first approximation) the nonlinear phase velocity would be of order $c_{f1}(1 + \frac{1}{2}a_f^2 k_f^2)$. In the present study, this corresponds to an increase of approximately 5% for the steepest wave group (i.e. case D with an input amplitude of $A = 55$ mm). Although this increase is larger than the uncertainty in the measuring technique, the data presented in figure 14 shows no observable increase in the phase velocity.

One possible explanation for this lies in the formation of a backwards (or negative) flow at the scale of the wave group. This was first identified by Longuet-Higgins & Stewart (1964), and has been discussed earlier in the context of the long-wave motion that is set-down (figures 12*c* and 13*c*). This flow is also of order $(ak)^2 c$, and it may happen that in the present case it almost exactly cancels with the increase in the phase velocity arising from the local nonlinear interactions occurring at the focused wave crest. Indeed, if the second-order wave–wave interactions (equation (2.5)) are incorporated within equations (5.1) and (5.2), there is no significant change in the predicted phase velocity.

In a subsequent investigation (initiated as a result of comments received during the review procedure), the phase velocity was measured for a variety of input parameters, including a range of wave heights, frequency bands and spectral shapes. In all cases, the second-order correction to the phase velocity was extremely small, and the measured data shown to be in good agreement with the linear solution. These results further suggest that, over the admittedly limited range of bandwidths appropriate to a laboratory wave flume, the two (opposing) nonlinear contributions to the velocity of the focused wave crest cancel, and as a result there is good agreement with the linear solution outlined in equations (5.1) and (5.2).

For each of the frequency bands described in table 1, the input amplitude was increased until the onset of wave breaking. This limiting condition was characterized by a progressive steepening of the largest wave crest and the eventual formation of a spilling breaker. In each case the onset of wave breaking occurred with an input amplitude of $A \approx 60$ mm. This corresponds to a limiting wave steepness of $Ak_c = 0.24$, which is very close to the value of $Ak_c = 0.25$ obtained by Rapp & Melville (1990). Figure 15 considers this limiting condition and compares the present data with the observations presented by Rapp & Melville (1990). The agreement between these data sets is somewhat surprising since the amplitude spectra used in the present study ($a(\sigma) \sim \sigma^{-2}$) are very different from the top hat distribution used by Rapp & Melville. Indeed, it remains unclear why a linear criterion, based upon a central wave number ($k_c$), should provide a good description of the limiting conditions within a highly nonlinear flow field in which the maximum crest elevation is strongly bandwidth dependent (figure 8).

The onset of wave breaking was further investigated using still photography. With the aid of an electronic trigger to control the camera shutter, a picture of the water surface elevation was obtained at the instant of wave focusing. Using this approach, it was estimated that the spatial variation in the water surface elevation could be determined to $\pm 3$ mm. If (as above) $a_f k_f$ defines the local wave steepness, where $a_f$ is half the instantaneous wave height and $k_f$ is the local wave number calculated from the measured wave length, then the onset of wave breaking occurs at $a_f k_f = 0.22$ and 0.34 for cases B and D, respectively. These values are considerable smaller than the limiting steepness for a regular wave train ($ak \approx 0.44$), and appear to be

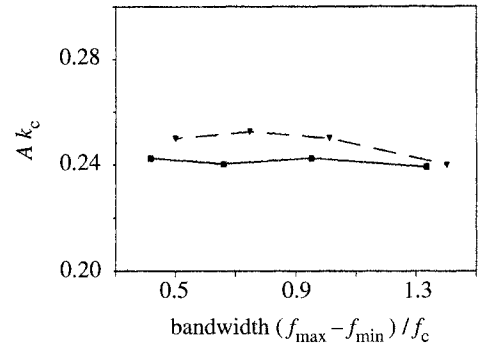


Figure 15. Limiting conditions for a focused wave group: — —, Rapp & Melville (1990), ——, present data.

Table 2. *Limiting wave characteristics*

| | experimental data | | | | linear theory | |
|---|---|---|---|---|---|---|
| | $\eta_{max}$ | $\eta_{min}$ | $k_f$ | $a_f$ | $\eta_{max}$ | $\eta_{min}$ |
| Case B | +76 mm | −14 mm | ≈ 5.2 | 45 mm | +60 mm | −24 mm |
| Case D | +92 mm | −39 mm | ≈ 5.2 | 66 mm | +60 mm | −46 mm |

consistent with the results presented by Rapp & Melville (1990). In particular, the limiting values of the locally measured wave amplitude (either $a_f$ or $\eta_{max}$) reduces with increasing bandwidth. Data describing the local wave characteristics at the onset of breaking are given in table 2.

This data highlights the extreme crest–trough asymmetry within the spatial domain, and suggests that although the onset of wave breaking occurs at large crest elevations ($\eta_{max}$), the corresponding local wave amplitudes ($a_f$) are relatively small. For example, a comparison with linear wave theory (see table 2) suggests that, with a broad-banded spectrum (case B), $a_f$ is only some 7% larger than that predicted by the linear sum of the wave components, whereas, in the narrow-banded spectrum (case D), $a_f$ is approximately 25% larger. However, in both cases, $a_f$ is significantly smaller than the limiting amplitude of an equivalent regular wave. For example, a Stokes wave having the same wave number ($k = k_f$) would have a predicted limiting amplitude of the order of 85 mm. This is almost twice as large as that observed in the broad-banded case (B), and 29% larger than the narrow-banded case (D).

### (*f*) *Spectral properties and relative phasing*

It is clear from the measurements of both the water surface elevation and the underlying kinematics that there is a redistribution of the energy within the focused wave group. To investigate this behaviour, the power spectrum of the recorded water surface elevation was determined via a fast Fourier transform (FFT). Unfortunately, this approach is not well suited to the analysis of an individual focusing event. The confidence limits associated with an FFT require the total signal length to be very much larger than the period of the component waves. As a result, the focusing event, within which the important nonlinearities occur, only occupies a small proportion of

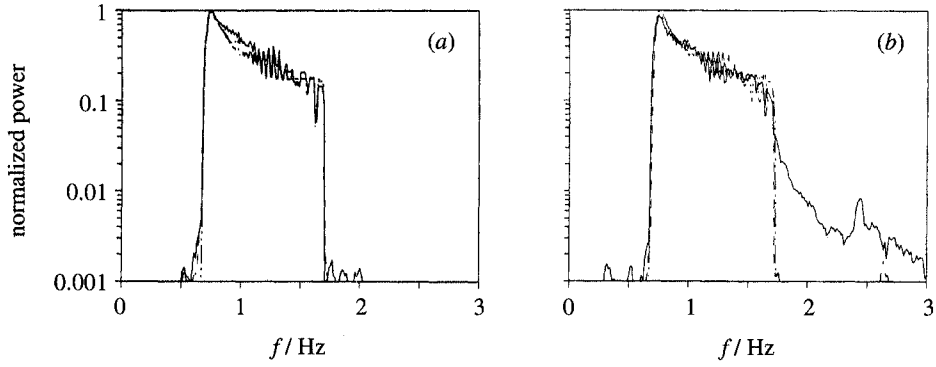


Figure 16. Power spectra estimates (case B, (*a*) $A = 22$ mm; (*b*) $A = 55$ mm): — - - —, numerical data input to wave paddle ($\eta(t)$ at $x = x_p$); — —, $\eta(t)$ at $x = -8$ m; ——, $\eta(t)$ at $x = 0$.

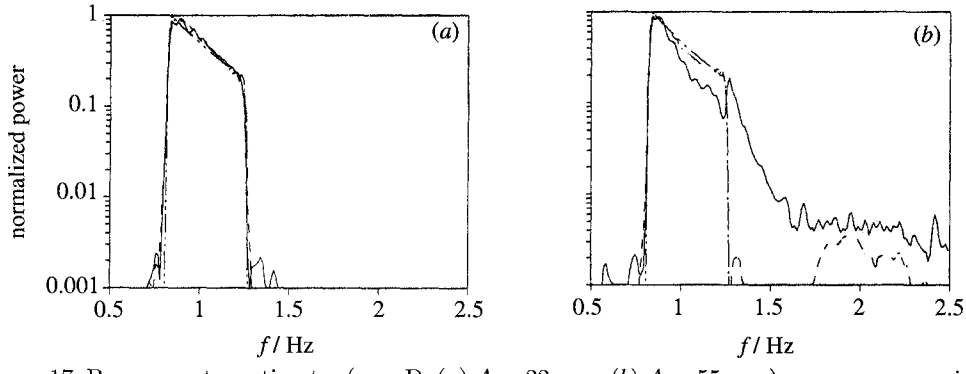


Figure 17. Power spectra estimates (case D, (*a*) $A = 22$ mm; (*b*) $A = 55$ mm): — - - —, numerical data input to wave paddle ($\eta(t)$ at $x = x_p$); — — —, $\eta(t)$ at $x = -8$ m; ———, $\eta(t)$ at $x = 0$.

the total signal length. Nevertheless, previous researchers (including Rapp & Melville 1990) have shown that important information can be obtained.

The results of the FFT analysis are shown on figures 16 and 17. In each case, the water surface elevation was sampled at 25 Hz for a duration of 82 s to give a total of 2048 data points. Figures 16*a*, *b* correspond to the broad-banded spectrum (case B) with an input amplitude of $A = 22$ mm and $A = 55$ mm, respectively. In each figure, three normalized power spectra are shown: the first is based upon the input signal sent to the wave paddle; the second corresponds to the surface elevation measured 8 m upstream of the focus position ($x = -8$ m); and the third is the power spectrum derived from the surface elevation measured at the focus point ($x_f = 0$). In each figure, the distribution of energy within a number of discrete wave components is indicated by the 'jagged' characteristics of the power spectra. In figure 16*a* ($A = 22$ mm), the measured data shows a small energy 'leakage' towards the low-frequency components, but there is no significant transfer of energy into the higher harmonics. In contrast, figure 16*b* ($A = 55$ mm) identifies a significant transfer of energy into the higher harmonics at the focus location.

Figures 17*a*, *b* present a similar sequence of plots for the narrow-banded spectrum (case D). In this case, the same number of wave components ($N = 29$) are generated within a smaller frequency range and, consequently, the normalized power spectra are smoother than those given previously. With an input amplitude of $A = 22$ mm, there

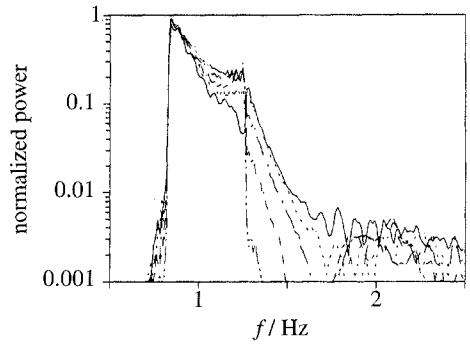


Figure 18. Spatial variation in power spectral estimates (case D, $A = 55$ mm): — - - —, $x = -8$ m; — —, $x = -6$ m; — - —, $x = -4$ m; - - -, $x = -2$ m; ——, $x = 0$ m.

is again no significant transfer of energy within the frequency domain. However, with a larger input amplitude (figure 17*b*), the power spectrum of the surface elevation measured 8 m upstream of the focus position shows the importance of the second harmonics (i.e. there is a significant energy distribution within the frequency range 1.7–2.3 Hz). In contrast, the power spectrum corresponding to the focus position shows a reduction of energy within the input frequency range (0.8–1.3 Hz), and a redistribution of this energy to the higher harmonics (> 1.3 Hz). Figure 18 shows the normalized power spectra of the surface elevation measured at five locations within the wave flume. The transfer of energy into the higher harmonics as the wave group approaches the focus position is clearly identified.

In addition to the spectral information discussed above, the relative phasing of the wave components can also be determined from a Fourier transform of the measured water surface elevation. Figures 19*a–i* concern the narrow-banded spectrum (case D) with an input amplitude of $A = 22$ mm. The relative phasing of the free waves is considered at seven locations fixed relative to the linear focus position. In each case, the measured data is in good agreement with a linear solution and, in particular, the waves are in phase at the predicted linear focus, i.e. $\Delta\psi = 0$ at $x = 0$ (figure 19*e*). In contrast, figures 20*a–i* again concern the narrow-banded spectrum (case D) and give a similar sequence of data corresponding to an input amplitude of $A = 55$ mm. In this latter case, the nonlinear wave–wave interactions change the relative phasing of the wave components. As a result, the waves are no longer in phase (i.e. $\Delta\psi \neq 0$) at the linear focus position (figure 20*e*). This is consistent with the previous measurements of the focus position given in figure 10*a*. These phase changes (relative to the linear solution) imply that the phase velocity of the wave components has changed. Indeed, figure 20*e* suggests that the dispersion within the wave group is reduced since the initial phase differences are decreasing more slowly in comparison with the low-amplitude case (figure 19*e*). These results are consistent with the notion that the wave components are becoming bound to the 'dominant' waves within the group.

To a first order of approximation, the group velocity is defined by $c_g = \mathrm{d}\omega/\mathrm{d}k$. After substituting for the phase velocity $c = \omega/k$, we obtain (from Tucker 1991)

$$c_g = c - \lambda \mathrm{d}c/\mathrm{d}\lambda, \tag{5.3}$$

where $\lambda$ is the wavelength. In the case of a regular wave train propagating in deep water, the final term in equation (5.3) reduces to $\frac{1}{2}c$ giving the well-known result that (to a first approximation) the group velocity is equal to one half of the phase velocity in deep water. However, in the present case, the experimental data suggests

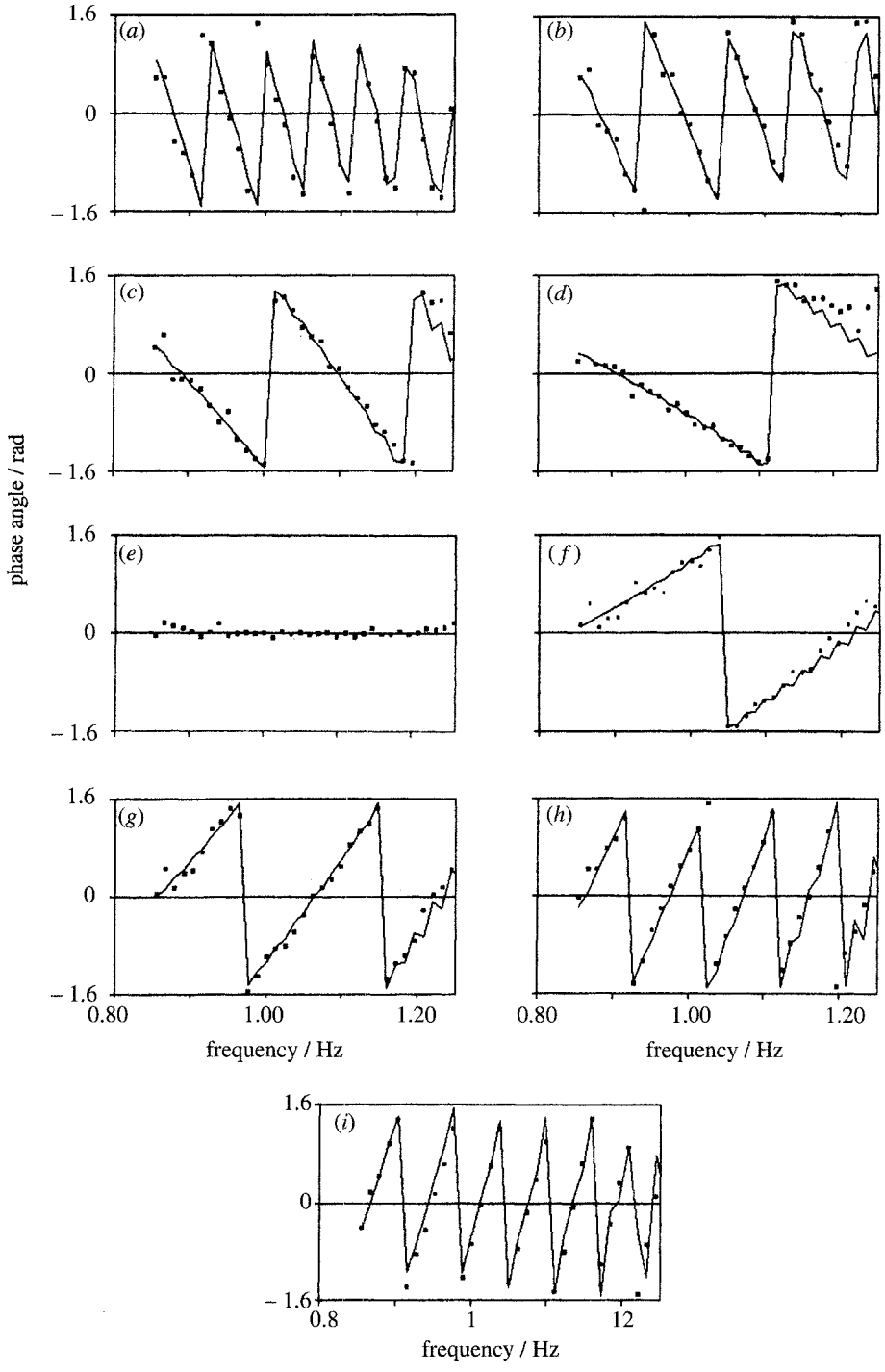


Figure 19. Phase changes along the length of the wave flume (case D, $A = 10$ mm, (*a*) $x = -6$ m; (*b*) $x = -4$ m; (*c*) $x = -2$ m; (*d*) $x = -1$ m; (*e*) $x = 0$ m; (*f*) $x = +1$ m; (*g*) $x = +2$ m; (*h*) $x = +4$ m; (*i*) $x = +6$ m): ——, linear phases; •, measured phases.

that the nonlinear interactions produce a relative change in the local phase velocity.

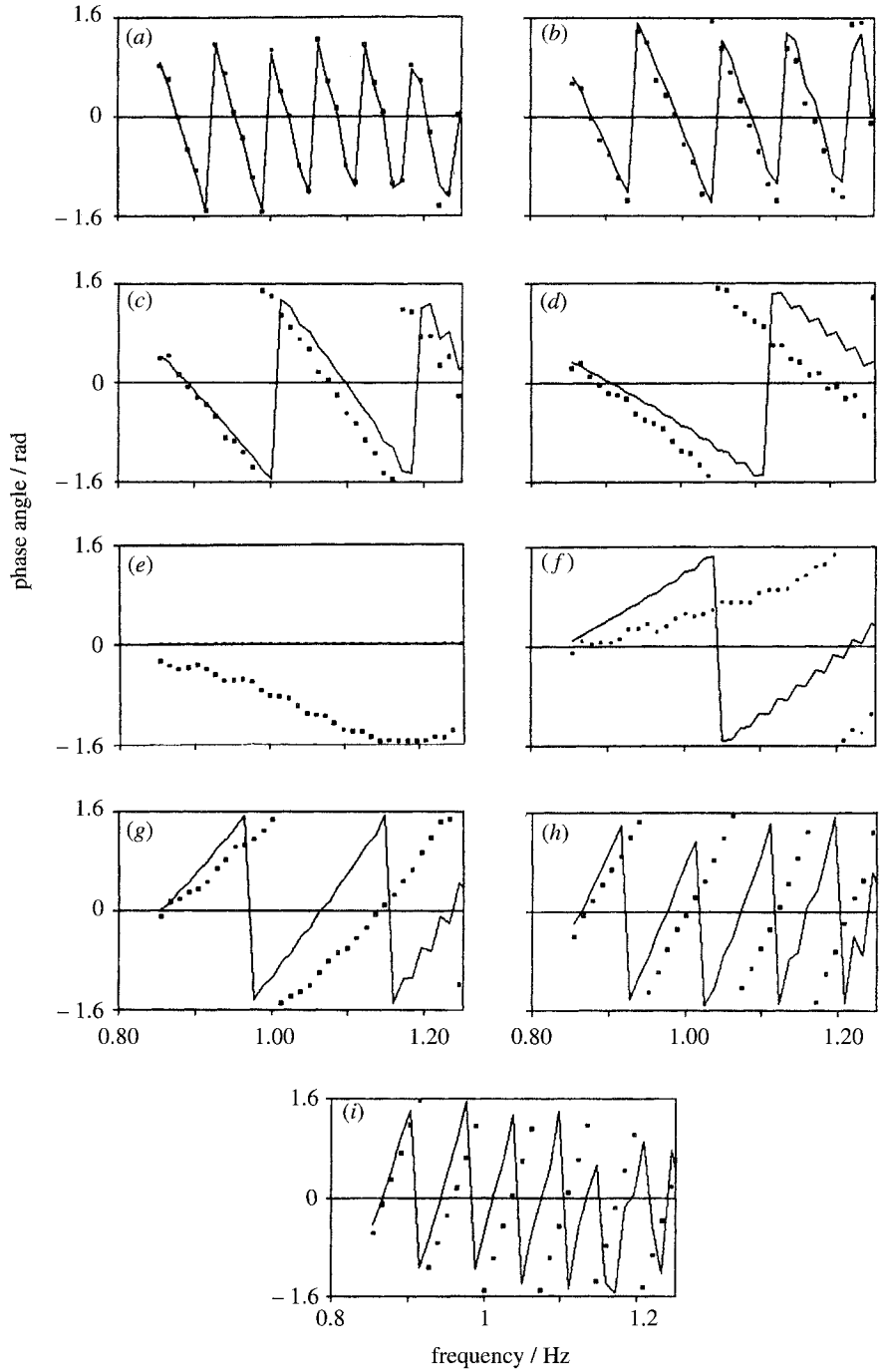


Figure 20. Phase changes along the length of the wave flume (case D, $A = 55$ mm, (*a*) $x = -6$ m; (*b*) $x = -4$ m; (*c*) $x = -2$ m; (*d*) $x = -1$ m; (*e*) $x = 0$ m; (*f*) $x = +1$ m; (*g*) $x = +2$ m; (*h*) $x = +4$ m; (*i*) $x = +6$ m): ——, linear phases; •, measured phases.

In particular, the phase changes identified via the Fourier transform suggest that the phase velocity of the high-frequency components is increased relative to that

of the low-frequency components (hence the reduced dispersion). Consequently, a nonlinear term arises in which $dc/d\lambda < 0$, and, as a result, equation (5.3) predicts an increase in the local group velocity. Although this argument is perhaps somewhat tenuous, not least because the nonlinear group velocity is not uniquely defined, the present results appear to be consistent with the theoretical investigation presented by Peregrine & Thomas (1979). Having considered a number of alternative definitions (based upon the propagation of wave energy and wave action), they concluded that for steep narrow-banded waves the nonlinear group velocity increases.

Finally, the experimental data gathered downstream of the focus position (figure 20*i*) suggest that the nonlinear interactions associated with the focusing of wave components produces a permanent phase change. This is perhaps consistent with the calculations presented by Oikawa & Yajima (1974), Yuen & Lake (1982) and Peregrine (1983), which have shown that the nonlinear interaction of solitons travelling at different velocities also produces a permanent phase change.

## 6. Conclusions and practical implications

A new series of experimental observations has been presented in which the water surface elevation and the underlying kinematics were measured for a range of two-dimensional wave groups. In each case, the individual wave components were focused at one point in space and time so that constructive interference occurred resulting in a large wave crest. A focusing event of this type is believed to be of considerable practical importance since it provides a realistic mechanism for the development of an extreme wave form appropriate to the design of offshore structures and vessels. If this event is specified in terms of a given return period (typically a 100 year design wave), both the maximum water surface elevation and the underlying kinematics are required to determine the associated fluid loads.

The present measurements have shown that the focusing of wave components can produce a highly nonlinear wave group in which both the water surface elevation and the near-surface water particle kinematics are significantly larger than that predicted by the linear sum of the wave components. In particular, the central wave crest (measured at the focus location) is higher and narrower, while the adjacent wave troughs are broader and less deep. These changes correspond to a steepening of the overall wave envelope, and suggest that there is an increase in the local energy density at the focus location. The experimental data indicates that the nonlinearity of the wave group increases with the amplitude of the wave components, but reduces with increasing bandwidth. This pattern is observed in both the maximum crest elevation and the downstream shifting of the focus location. However, in this latter case, it is interesting to note that the summation of $N$ wave crests are focused at exactly the same location as $N$ wave troughs. This implies that the focusing of wave energy is dependent upon the overall nonlinearity of the wave group (i.e. an envelope effect) and is not dependent upon the 'local' interactions occurring at the focus location.

A second-order solution based upon the sum of the wave–wave interactions terms identified by Longuet-Higgins & Stewart (1960) has also been presented. Comparisons with the experimental data suggest that, although this solution provides an improved description of the water surface elevation, many of the wave–wave interactions occur at a higher order of wave steepness. This is consistent with the numerical calculations presented by Longuet-Higgins (1987). In particular, the bandwidth dependence clearly identified in the experimental data does not arise at a second order

of wave steepness. Indeed, the velocity data provides further evidence as to the importance of the higher order interactions. In the narrow-banded spectrum, the near surface velocities are considerably larger then either the first- or the second-order solutions based upon the input wave components. This result is at odds with a number of previous experimental studies (notably Skjelbreia *et al.* 1991), which suggest that an extrapolated linear solution will overestimate the magnitude of the near-surface velocities in a random wave train. Indeed, these experimental results have led to the formulation of several empirically modified (or stretched) wave theories. These are widely used in the offshore industry and are specifically adapted to reduce the magnitude of the predicted velocities within the crest to trough region. However, the present study shows that in the case of a focused wave group the nonlinear interactions may produce very large near-surface velocities which are inconsistent with the existing empirical formulations. The experimental data also suggests that the nonlinear interactions produce a velocity reduction in the lower layers of the flow field. This is particularly apparent in the broad-banded spectrum and is believed to be associated with a long bound wave. This produces a backwards (or negative) flow on the scale of the wave group, and may be interpreted as a dynamic response to the positive mass transport occurring beneath the focused wave group. This long-wave interaction first arises at a second order of wave steepness, and is shown to be in good agreement with the solution proposed by Longuet-Higgins & Stewart (1960).

In contrast to the nonlinearity observed in both the water surface elevation and the underlying kinematics, the phase velocity of the focused wave crest is shown to be in good agreement with linear theory. The most likely explanation for this is that the expected nonlinear increase in the local phase velocity is offset by the negative flow associated with the low-frequency modulation (or set-down) of the mean water level. The spectral properties of the focused wave group (determined from a Fourier analysis of the recorded water surface elevation) indicate that the nonlinear interactions lead to a significant transfer of energy into the higher harmonics. This provides the large increase in the local energy density, which is consistent with the change in the surface profile. Provided there is no evidence of wave breaking, these energy changes appear to be entirely reversible; in the sense that the wave group is symmetric about the focus location. In addition, the Fourier analysis also describes the relative phasing of the wave components, and shows that the dispersion of the wave group is reduced by the nonlinear interactions. This accounts for the downstream shifting of the focus location, and implies that there is a nonlinear increase in the group velocity. This latter point is consistent with the theoretical calculations presented by Peregrine & Thomas (1979). The phasing of the wave components also suggests that the free waves undergo a permanent phase change in regions of high nonlinearity. This is perhaps analogous to the phase changes which occur when solitons of different velocity interact nonlinearly.

Finally, the present study also considered the limiting characteristics of the focused wave groups. In each case, the onset of wave breaking was found to occur at $Ak_c \approx 0.24$, which is very close to the value of $Ak_c \approx 0.25$ identified by Rapp & Melville (1990). The agreement between these results is somewhat surprising since the spectral properties of the wave groups show considerable variation. Indeed, given that much of the present experimental data suggests that a focused wave group is both highly nonlinear and bandwidth dependent, it is difficult to explain why a linear criterion, based upon a central wave number, should provide such a good representation of the limiting condition.

The authors gratefully acknowledge the financial support provided by the Engineering and Physical Sciences Research Council (EPSRC), The Royal Society (under the Research Grants Scheme) and Shell UK Exploration and Production Ltd.

## Appendix A.

The second-order constants ($C$, $D$, $E$ and $F$) introduced in equations (2.1) and (2.2) are given by Longuet-Higgins & Stewart (1960) as

$$C = \frac{[2\sigma_1\sigma_2(\sigma_1-\sigma_2)(1+\alpha_1\alpha_2)+\sigma_1^3(\alpha_1^2-1)-\sigma_2^3(\alpha_2^2-1)](\sigma_1-\sigma_2)(\alpha_1\alpha_2-1)}{\sigma_1^2(\alpha_1^2-1)-2\sigma_1\sigma_2(\alpha_1\alpha_2-1)+\sigma_2^2(\alpha_2^2-1)} + (\sigma_1^2+\sigma_2^2)-\sigma_1\sigma_2(\alpha_1\alpha_2+1), \tag{A 1}$$

$$D = \frac{[2\sigma_1\sigma_2(\sigma_1+\sigma_2)(\alpha_1\alpha_2-1)+\sigma_1^3(\alpha_1^2-1)+\sigma_2^3(\alpha_2^2-1)](\sigma_1+\sigma_2)(\alpha_1\alpha_2+1)}{\sigma_1^2(\alpha_1^2-1)-2\sigma_1\sigma_2(\alpha_1\alpha_2+1)+\sigma_2^2(\alpha_2^2-1)}, -(\sigma_1^2+\sigma_2^2)+\sigma_1\sigma_2(\alpha_1\alpha_2-1), \tag{A 2}$$

$$E = -\tfrac{1}{2}a_1a_2[2\sigma_1\sigma_2(\sigma_1-\sigma_2)(1+\alpha_1\alpha_2)+\sigma_1^3(\alpha_1^2-1)-\sigma_2^3(\alpha_2^2-1)], \tag{A 3}$$

$$F = -\tfrac{1}{2}a_1a_2[2\sigma_1\sigma_2(\sigma_1+\sigma_2)(1-\alpha_1\alpha_2)-\sigma_1^3(\alpha_1^2-1)-\sigma_2^3(\alpha_2^2-1)], \tag{A 4}$$

where $\lambda$ represents the ratio of the wave frequencies ($\sigma_2/\sigma_1$) and the $\alpha$ coefficients are

$$\alpha_1 = \coth(k_1h), \quad \alpha_2 = \coth(k_2h). \tag{A 5}$$

## References

Fenton, J. D. 1985 A fifth order Stokes theory for steady waves. *J. Waterways Port Coastal Ocean Engng* **111**, 216–234.

Forristall, G. Z. 1986 Kinematics in the crest of storm waves. In *Proc. 20th Int. Conf. on Coastal Engineering* (Taipei), vol. 1, pp. 193–207. ASCE.

Gudmestad, O. T. & Connor, J. J. 1986 Engineering approximation to nonlinear deep water waves. *App. Ocean Res.* **8**, 76–88.

Gudmestad, O. T. 1990 A new approach for estimating irregular deep water wave kinematics. *App. Ocean Res.* **12**, 20–24.

Kim, C. H., Randall, R. E., Boo, S. Y. & Krafft, M. J. 1992 Kinematics of 2D transient water waves using Laser Doppler anemometry. *J. Waterways Port Coastal Ocean Engng* **118**, 147–165.

Kinsman, B. 1984 *Wind waves. Their generation and propagation on the ocean surface.* 2nd edn. New York: Dover.

Longuet-Higgins, M. S. 1952 On the statistical distribution of the heights of sea waves. *J. Marine Res.* **11**, 245–266.

Longuet-Higgins, M. S. & Stewart, R. W. 1960 Changes in the form of short gravity waves on long waves and tidal currents. *J. Fluid Mech.* **8**, 565–583.

Longuet-Higgins, M. S. & Stewart, R. W. 1964 Radiation stresses in water waves; a physical discussion, with applications. *Deep-Sea Res.* **11**, 529–562.

Longuet-Higgins, M. S. 1974 Breaking waves—in deep or shallow water. In *Proc. 10th. Conf. on Naval Hydrodynamics* (Cambridge, MA), pp. 597–605.

Longuet-Higgins, M. S. 1980 On the distribution of the heights of sea waves: some effects of nonlinearity and finite bandwidth. *J. Geophys. Res.* **85**, 1519–1523.

Longuet-Higgins, M. S. 1987 The propagation of short surface waves on longer gravity waves. *J. Fluid Mech.* **177**, 293–306.

Miller, S. J., Shemdin, O. R. & Longuet-Higgins, M. S. 1991 Laboratory measurements of the modulation of short wave slopes by long surface waves. *J. Fluid Mech.* **233**, 389–404.

Oikawa, M. & Yajima, N. 1974 A perturbation approach to nonlinear systems. 2 Interaction of nonlinear modulated waves. *J. Phys. Soc. Japan.* **37**, 486–496.

Peregrine, D. H. & Thomas, G. P. 1979 Finite-amplitude deep-water waves on currents. *Phil. Trans. R. Soc.* A **292**, 371–390.

Peregrine, D. H. 1983 Water waves, nonlinear Schrödinger equations and their solutions. *J. Austral. Math. Soc.* B **25**, 16–43.

Rapp, R. J. & Melville, W. K. 1990 Laboratory measurements of deep water breaking waves. *Phil. Trans. R. Soc.* A **331**, 735–800.

Rodenbusch, G. & Forristall, G. Z. 1986 An empirical method for random directional wave kinematics near the free surface. In *Proc. 18th Annual Offshore Technology Conf.* (Houston, TX), vol. 1, pp. 137–146.

Schaffer, A. M. 1993 Laboratory wave generation correct to second-order. Wave kinematics and environmental forces. *Proc. Soc. Underwater Technol.* **29**, 115–139.

Skjelbreia, J., Berek. E., Bolen, J. K., Gudmestad, O. T., Heideman,J., Ohmart, R. R., Spidsoe, N. & Torum, A. 1991 Wave kinematics in irregular waves. *Proc. Offshore Mech. and Arctic Eng. OMAE.* (Stavanger), vol. 1, pp. 233–228. New York: ASME.

Slepian, D. 1963 On the zeros of Gaussian noise. In *Time series analysis* (ed. M. Rosenblatt), pp. 104–115. New York: Wiley.

Sobey, R. J. 1990 Wave theory predictions of crest kinematics. In *Water wave kinematics* NATO ASI Ser. 178 (ed. A. Torum & O. T. Gudmestad), pp. 215–231.

Stokes, G. G. 1847. On the theory of oscillatory waves. *Trans. Camb. Phil. Soc.* **8**, 441–455.

Swan, C. 1990. Convection within an experimental wave flume. *J. Hydraulic Res.* **28**, 273–282.

Taylor, P. H. 1992. On the kinematics of large ocean waves. In *Proc. 6th Int. Conf. on the behaviour of offshore structures (BOSS)* (London), vol. 1, pp. 134–145.

Tromans, P. S., Anaturk, A. & Hagemeijer, P. 1991 A new model for the kinematics of large ocean waves—application as a design wave. In *Proc. 1st Int. Conf. Offshore and Polar Engineering* (Edinburgh), vol. 3, pp. 64–71.

Tucker, M. J. 1991 *Waves in ocean engineering: measurement, analysis, interpretation.* Chichester: Ellis Horwood.

Wheeler, J. D. 1970 Method for calculating forces produced by irregular waves. In *Proc. 1st Annual Offshore Technology Conf.* (Houston), vol. 1, pp. 71–82.

Yuen, H.C., & Lake, B.M. 1982. Nonlinear dynamics of deep-water gravity waves. In *Advances in applied mechanics* (ed. Chia-Shun Yih) vol. 22, pp. 153-180. London: Academic.

*Received 17 August 1994; accepted 8 February 1995*